RESEARCH ARTICLE

4D Printing of Overall Radiopaque Customized Bionic Occlusion Devices

Cheng Lin, Zhipeng Huang, Qinglong Wang, Zhichen Zou, Wenbo Wang, Liwu Liu,* Yanju Liu, and Jinsong Leng*

Percutaneous closure of ventricular septal defect (VSD) can effectively occlude abnormal blood flow between ventricles. However, commonly used Nitinol occlusion devices have non-negligible limitations, such as nondegradability leading to life-threatening embolization; limited device size predisposing to displacement and wear; only a few radiopaque markers resulting in inaccurate positioning. Nevertheless, the exploration of customized, biodegradable, and overall radiopaque occluders is still vacant. Here, overall radiopaque, biodegradable, and dynamic reconfigurable 4D printed VSD occluders are developed. Based on wavy bionic structures, various VSD occluders are designed and manufactured to adapt to the position diversity of VSD. The customized configuration, biocompatibility, and biodegradability of the developed 4D printed bionic occluders can eliminate the series of complications caused by traditional occluders. The overall radiopacity of 4D printed VSD occluders is validated ex vivo and in vivo, whereby accurate positioning can be assured. Notably, the preparation strategies for 4D printed occluders are scalable, eliminating the barriers to mass production, and marking a meaningful step in bridging the gap between modeling and clinical application of 4D printed occlusion devices. This work opens attractive perspectives for the rapid manufacturing of customized intelligent medical devices for which overall radiopacity, dynamic reconfigurability, biocompatibility, and biodegradability are sought.

C. Lin, J. Leng
Centre for Composite Materials and Structures
Harbin Institute of Technology
No. 2 Yikuang Street, Harbin 150001, P. R. China
E-mail: lengjs@hit.edu.cn

L. Liu, Y. Liu
Department of Astronautical Science and Mechanics
Harbin Institute of Technology
No. 92 West Dazhi Street, Harbin 150001, P. R. China
E-mail: liulw@hit.edu.cn

Z. Huang, Q. Wang
Tangdu Hospital of the Air Force Military Medical University
No. 1, Xinsi Road, Xi'an 710038, P. R. China

Z. Zou, W. Wang
The First Affiliated Hospital of Harbin Medical University
No. 23 Youzheng Street, Nangang District, Harbin 150001, P. R. China

1. Introduction

A ventricular septal defect (VSD) is an opening in the ventricular septum that causes an abnormal hemodynamic connection between the two ventricles (**Figure 1**). VSD is the most common congenital cardiac malformation in children, accounting for 0.2% to 0.6% of all live births.[1,2] The VSD allows the oxygen-rich blood to flow from the left ventricle to the right ventricle through the opening and mix with deoxygenated blood in the right ventricle, which may lead to severe complications, such as arrhythmia, ventricular dysfunction, and pulmonary hypertension. The case of percutaneous closure of VSD was first reported by Lock et al. in the 1980s.[3] Subsequently, the development of VSD occluders (VSDOs) and the tremendous advances in percutaneous and imaging technologies have further expanded the application of percutaneous closure in VSD, enabling more positive results in closing VSDs.[4–10] Due to less invasiveness and rapid postoperative surgery, percutaneous closure of VSD provides an effective alternative to open surgery and has become the preferred treatment for specific VSD patients.[4]

Ideally, VSDOs are a temporary medium that should disappear when the defect is endothelized and replaced by autologous tissue.[11–13] Whereas the current alloy VSDOs are woven from nondegradable nitinol wires and covered with nondegradable polymer patches. Although these alloy VSDOs are effective in blocking abnormal blood flow at the ventricular level, nonnegligible complications regarding alloy occluders have been reported. For example, nondegradability leads to late displacement and life-threatening embolism; allergy caused by nickel ion precipitation; perforation and tamponade due to long-term mechanical wear; delayed endothelialization due to limited biocompatibility. In addition, only a few X-ray markers on the device may cause inaccurate positioning and affect the efficacy of occlusion.[14–23] Therefore, it is of great significance to develop biodegradable and overall radiopaque occluders to reduce complications and improve occlusion performance. Biodegradable biopolymer occluders can completely and effectively avoid the late complications caused by alloy occluders. However, the current exploration of biodegradable VSDOs is extremely insufficient. Qin et al. developed

**ADVANCED
SCIENCE NEWS**

www.advancedsciencenews.com

**ADVANCED
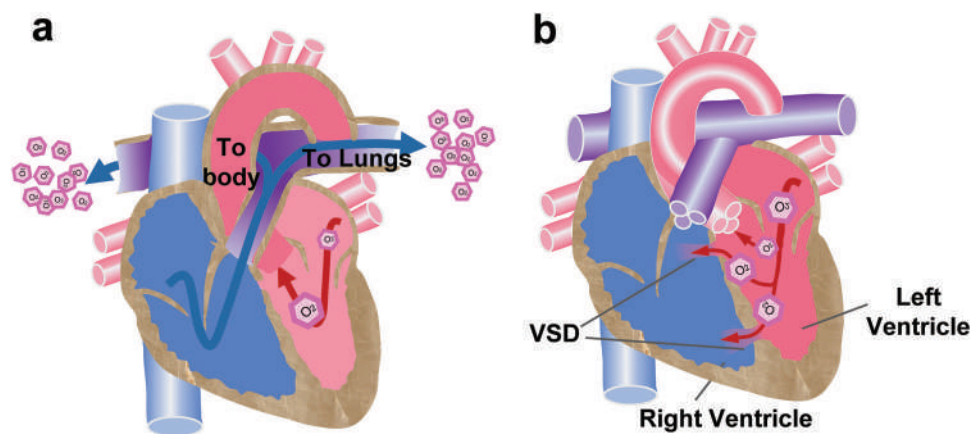HEALTHCARE
MATERIALS**

www.advhealthmat.de

Figure 1. Blood flow directions of a) normal heart and b) heart with ventricular septal defect (VSD).

biodegradable VSDOs using polydioxanone (PDO) monofilaments, but the occluders lacked overall radiopacity.[24] Moreover, the occluders were still prepared by the traditional weaving method. Since there were only a few specific sizes of occluders that require the patient to fit the device, complications (e.g., displacement, wear) may occur due to mismatch.

Fortunately, three-dimensional (3D) printing can create implants with unprecedented complexity and precision, allowing implants to accurately fit the anatomy of the recipient in ways that are not feasible (or difficult to achieve) with traditional manufacturing techniques. 3D printing is a technology for producing constructs by adding materials in layers. It has developed at an impressive speed and has revolutionized the prototyping process of many fields, including aerospace, industrial manufacturing, and especially biomedicine. However, the static nature of 3D printed constructs greatly limits the possibility of actively controlling the performance of printed constructs. Instead, four-dimensional (4D) printing adds an additional spatial or temporal transformation dimension to 3D printing through environmental stimuli, thus enabling the shape transformation and functional evolution of the printed constructs.[25,26] 4D printing can be realized by integrating 3D printing and intelligent materials, and shape memory polymers (SMP) have become an attractive 4D printing intelligent material due to their exclusive programmable switchability and high processability.[27–30] 4D printed shape memory intelligent materials have been widely used in medical devices. For example, biocompatible and photosensitive 4D printed shape memory nanocomposites were prepared by incorporating gold nanoparticles into the shape memory polyurethane matrix. The nanocomposites exhibited excellent photothermal effects and enabled locally controllable breast tumor ablation.[28] In addition, remotely controllable and biodegradable cardiac occlusion devices were developed based on 4D printed shape memory magnetic nanocomposites, demonstrating outstanding shape memory performance and deformability.[12]

Herein, the objective of this work was to develop customized, biodegradable, and overall radiopaque occluders to avoid the migration, late embolization, and inaccurate positioning problems caused by conventional occluders. 4D printing was introduced into the preparation of the novel occluders that not only enabled the patient-tailored configuration but also enabled the

minimally invasive implantation process and self-adaptive deployment. First, 4D printed shape memory polyethylene glycol (PEG)/polylactic acid (PLA) biocomposites capable of shape transformation at near body temperature were prepared. To address the problem of inaccurate positioning of current occluders due to only a few X-ray markers, overall radiopaque 4D printing biocomposite filaments were prepared by introducing the barium sulfate ($BaSO_4$) radiopaque fillers into the shape memory PEG/PLA matrix. **Figure 2** displays the schematic workflow for fabricating and characterizing biodegradable, customized, and overall radiopaque 4D printed bionic occluders. Wavy bionic structures that can imitate the mechanical response of biological tissue were employed as the occluder disc structure. The configurations of the occluders were designed to be symmetrical, thin waist-large disc, eccentric, and elongated-waist to accommodate the defects in different positions and reduce the impact on the surrounding tissue. The occluders were prepared using the 4D printed $BaSO_4$-PEG/PLA biocomposite filaments through fused deposition modeling (FDM). FDM, a manufacturing method for creating 3D components by extruding thermoplastic filaments in continuous layers, was selected from a variety of 3D printing technologies. Since FDM can eliminate the need for toxic organic solvents or photosensitive resins, the risk of toxicity and barriers to the clinical application can be avoided. The mechanical properties, biodegradability, and biocompatibility of the 4D printed bionic occluders were systematically evaluated. Besides, the dynamic reconfigurable transformation capability of the 4D printed bionic occluders was examined, which validated the feasibility of minimally invasive treatment and controlled deployment. Finally, the overall radiopaque capabilities of various bionic occluders and the radiopaque performance under tissue interference in vivo were examined.

2. Results and Discussion

2.1. Characterization of 4D Printed Shape Memory Radiopaque Biocomposites

Radiopaque $BaSO_4$-PEG/PLA biocomposites with $BaSO_4$ contents of 5 wt%, 10 wt%, and 15 wt% were prepared, abbreviated

**ADVANCED
SCIENCE NEWS**

www.advancedsciencenews.com

**ADVANCED
HEALTHCARE
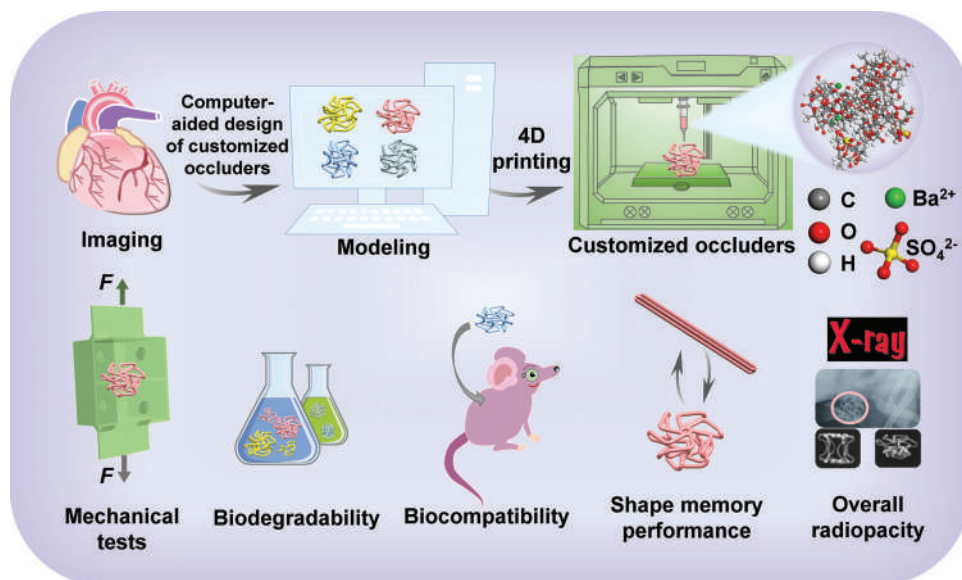MATERIALS**

www.advhealthmat.de

Figure 2. Schematic workflow for fabricating and characterizing biodegradable, customized, and overall radiopaque four-dimensional (4D) printed bionic occluders.

as 5BS-C, 10BS-C, and 15BS-C. To obtain the transition temperature of BS-C, differential scanning calorimetry (DSC) analysis was performed (**Figure 3**a). The transition temperatures of 5BS-C, 10BS-C, and 15BS-C were approximately 44 °C ± 3 °C, of which the transition temperature of 10BS-C was 43.39 °C. The transition temperature decreased substantially in BS-C compared to pure PLA (≈65 °C),[27] because the plasticization effect of PEG reduced the interaction between the PLA molecular chains. Therefore, BS-C not only avoided the possible negative effects of the high transition temperature of PLA implants on tissues but also maintained sufficient mechanical properties due to its glassy state at body temperature.[31] Figure 3b shows the Fourier-transform infrared spectroscopy (FT-IR) spectra of BS-C. The stretching and bending vibration peaks of $-CH_3$ were shown at approximately 2884 and 1359 cm^{-1}. The peaks at 1182 and 1084 cm^{-1} were attributed to the C−O−C vibration, and the vibration at 1455 cm^{-1} was characteristic of the vibration of −CH. In addition, it can be clearly observed that compared with the vibrational peaks of the PEG-PLA matrix without $BaSO_4$ (Figure S1, Supporting Information), BS-C presented a new absorption peak at 1043 cm^{-1}, which was the vibrational peak of sulfate. The stretching and bending vibration peaks of $-CH_3$ and the vibration peak of −CH were shifted to the right by approximately 8, 1, and 2 cm^{-1}, respectively.

The BS-C will serve as the printing raw material for implantable occluders, and therefore the mechanical properties of BS-C were characterized near the human temperature (32 °C, 37 °C, and 42 °C). At 32 °C, the tensile strengths of 5BS-C, 10BS-C, and 15BS-C were all approximately 12.5 MPa (Figure 3c–e). At 37 °C, the elongation at break increased and the tensile strength of 5BS-C, 10BS-C, and 15BS-C decreased slightly (12.0, 10.9, and 7.9 MPa, respectively). When the temperature rose to 42 °C, the elongation at break of BS-C continued to increase, and the strength/elongation at break of 5BS-C was 64.2%/11.3 MPa. The rigid radiopaque particles in BS-C were detached from the

polymer matrix during loading, and the micropores had more opportunities to develop into massive crazing, which was one of the mechanisms of toughening polymers.[32] Overall, 15BS-C exhibited the lowest tensile strength and toughness, possibly due to agglomeration caused by excessive radiopaque filler content. The toughness of 10BS-C was significantly better compared to the other two BS-Cs, probably due to its superior melting extrusion processability and printability. To simulate the evolution of the mechanical properties of BS-C after implantation, ex vivo biodegradation experiments were performed on BS-C (Figure 3f,g). On the whole, the elongation at break of BS-C decreased with the degradation time, while the tensile strength of BS-C showed a trend of first increasing and then decreasing with the degradation time. After 15 days of degradation, the tensile strengths of both 5BS-C and 10BS-C were about 21 MPa at 37 °C, while the tensile strength of 15BS-C was about 26 MPa. When the degradation time increased to 30 days, the tensile strengths of 5BS-C, 10BS-C, and 15BS-C were 16, 15, and 12 MPa, respectively. In addition, the flexural performance of the BS-C was analyzed by three-point bending tests. 5BS-C, 10BS-C, and 15BS-C all exhibited excellent flexural behaviors (Figure 3h), with only deformation occurring without significant damage over the loading range. Similar to the tensile behaviors, with the increase of degradation time, the elongation at break decreased with the degradation time, while the flexural strength first increased and then decreased (Figure 3i,j). After 15 days of degradation, the flexural strengths of 5BS-C, 10BS-C, and 15BS-C were 24.5, 21.5, and 18.0 MPa, respectively. The biodegradability of BS-C was verified by the weight loss of tensile and bending specimens. With the increase of degradation time, the weight loss rates gradually increased. The degradation rate of 5BS-C was faster than that of 10BS-C and 15BS-C, and the degradation rates of tensile and bending specimens were close for the same BS-C (Figure 3k,l). As the degradation time increased to 60 days, the weight loss rates of 5BS-C, 10BS-C, and 15BS-C tensile/bending specimens were
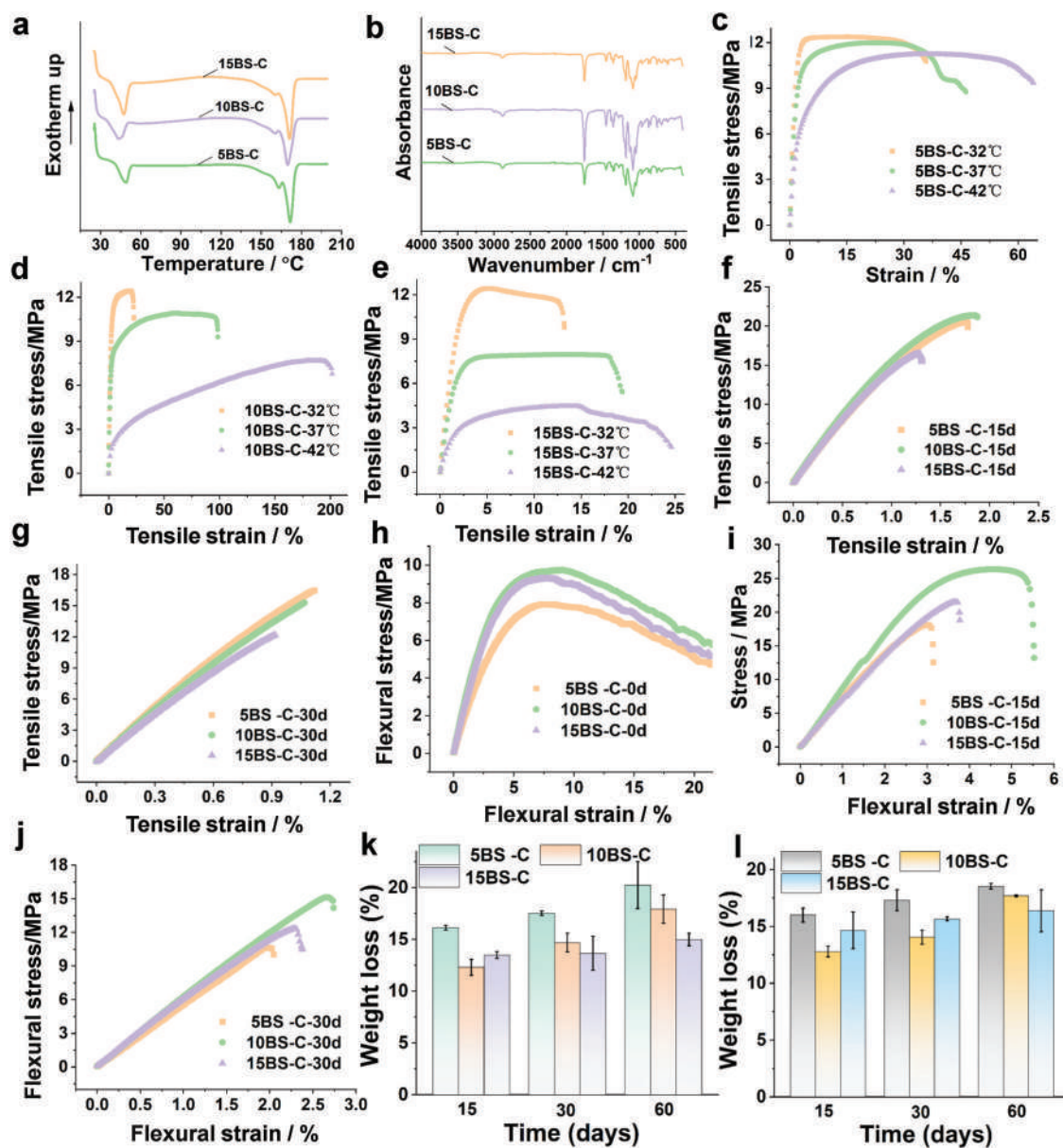
Figure 3. a) Differential scanning calorimetry (DSC) curves of BS-C. b) Fourier-transform infrared (FT-IR) spectra of BS-C. c–e) Tensile tests of BS-C at different temperatures. c) 5BS-C, d) 10BS-C, e) 15BS-C. Tensile tests of BS-C at 37 °C after f) 15 days and g) 30 days of degradation. Flexural performance of BS-C after h) 0 days, i) 15 days, and j) 30 days of degradation. k) Weight loss behavior of BS-C tensile samples. l) Weight loss behavior of BS-C flexural samples.

20.2%/18.5%, 17.9%/17.7%, and 15.0%/16.4%, respectively. The weight loss of BS-Cs demonstrated their biodegradability, providing a basis for the preparation of biodegradable VSDOs.

The shape transformation capability of the 4D printed BS-C constructs was investigated. Snowflake and polygonal network structures were prepared (**Figure 4**a1,b1). The two printed structures were allowed to be programmed to the badminton-like and mini-robot-like structures (Figure 4a2,b2), demonstrating the flexibility of programmed temporary shapes. The two structures in the temporary configuration can recover to the original configuration in an orderly manner under external stimuli, which showed excellent shape transformation behaviors.

2.2. Design and Fabrication of 4D Printed Bionic VSDOs

The mismatch between the mechanical properties of the occluder and biological tissue may aggravate tissue wear and even lead to perforation. The wave-shaped network structure can exhibit "J"-shaped stress–strain behavior similar to that of biological tissues, which is able to achieve cooperative deformation with biological tissues. Therefore, the introduction of wavy bionic structures into the structural design of the occluder will effectively reduce the risk of tissue wear.

Four wavy networks were developed and used as the basis for the structural design of VSDO discs. The four wavy networks

**ADVANCED
SCIENCE NEWS**

www.advancedsciencenews.com

**ADVANCED
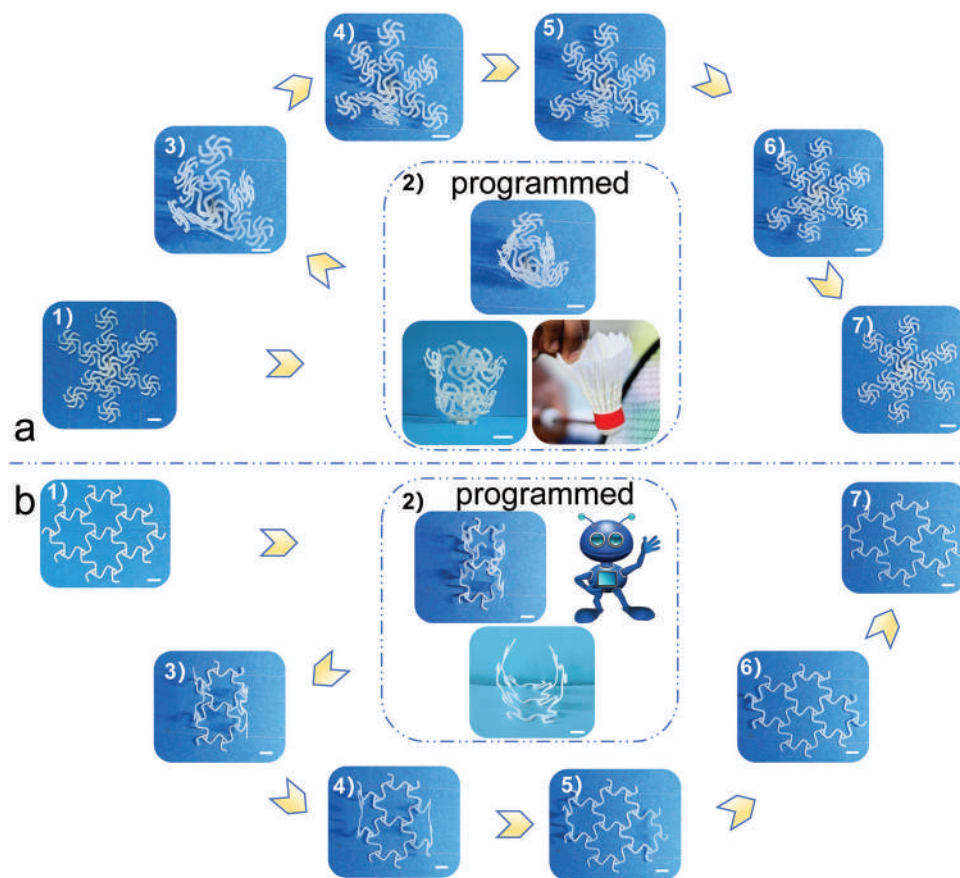HEALTHCARE
MATERIALS**

www.advhealthmat.de

Figure 4. Shape transformation behaviors of four-dimensional (4D) printed BS-C architectures. a1,b1) Initial configurations. a2,b2) Temporary configurations. a2–a7,b2–b7) Shape recovery processes. a7,b7) Recovered configurations. Scale bar: 10 mm.

included two ligament types (I and II) and two ligament numbers (six ligaments and three ligaments). Specifically, there were four types of representative units: type I-six ligament (I-u6), type I-three ligament (I-u3), type II-six ligament (II-u6), and type II-three ligament (II-u3). **Figure 5**a shows the geometric parameters of four wavy networks and representative units. The dimensionless geometric parameters determining the mechanical properties of the networks were $\theta = \pi/2$, $D/l = 0.171$, $\varnothing/l = 0.079$, $r/l = 0.107$. Correspondingly, the occluder disc was divided into four types: VSDOI-u6, VSDO II-u6, VSDOI-u3, and VSDO II-u3.

Compared with other congenital heart defects, VSD is characterized by higher incidence and diverse defect sites. Based on the anatomical location on the septum, VSD can be divided into four main types (Figure 5b), including outlet (infundibular) VSD, inlet (atrioventricular canal) VSD, muscular (trabecular) VSD (mVSD), and membranous VSD. Membranous VSD is the most common in the neonatal series, occurring in 80% of all VSD, and is also commonly known as perimembranous VSD (pmVSD).[33] Therefore, to further improve the success rate of occlusion and reduce the impact on surrounding tissues, VSDOs with different configurations were designed for VSDs in different anatomical locations, including symmetrical VSDO (S-VSDO), slender-waist VSDO (TW-VSDO), eccentric VSDO (Ee-VSDO), and muscle VSDO (m-VSDO) (Figure 5c). Among them, S-VSDO was suitable for the VSD that was more than 2 mm away from the

aortic valve; the TW-VSDO was suitable for blocking the multi-fenestrated VSD. The left disc diameter was 1.2 times that of the right disc, and the waist diameter was 0.8 times that of the left disc. By placing the thin waist of the occluder in the center of the defect, the large left disc can cover more defects in a large area; if the aortic stump was less than 2 mm, Ee-VSDO was an appropriate choice to avoid aortic valve compression; the m-VSD had a lengthened waist and was suitable for thicker muscular interventricular septum. Implantation of the occluder into the defect can close the VSD and allow oxygen-rich blood flow in the correct direction, Figure 5d illustrates the schematic of Ee-VSDO and m-VSD occluding the defect at different locations. Different types of VSDOs were prepared by 4D printing using BS-C radiopaque biocomposite filaments, and the printed occluders can accurately reproduce the configurations of the designed occluders (**Figure 6**a). PLA nonwoven membranes were used as blocking membranes and stitched on the printed occluder frame. Figure 6b shows the four membrane-covered occluders and their lightweight displays.

2.3. Overall Radiopacity of 4D Printed Bionic VSDOs

The radiopacity of VSDOs with different contents of radiopaque fillers was examined (**Figure 7**). Under X-rays, when the content of the radiopaque filler was increased to 5 wt%, the radiopacity
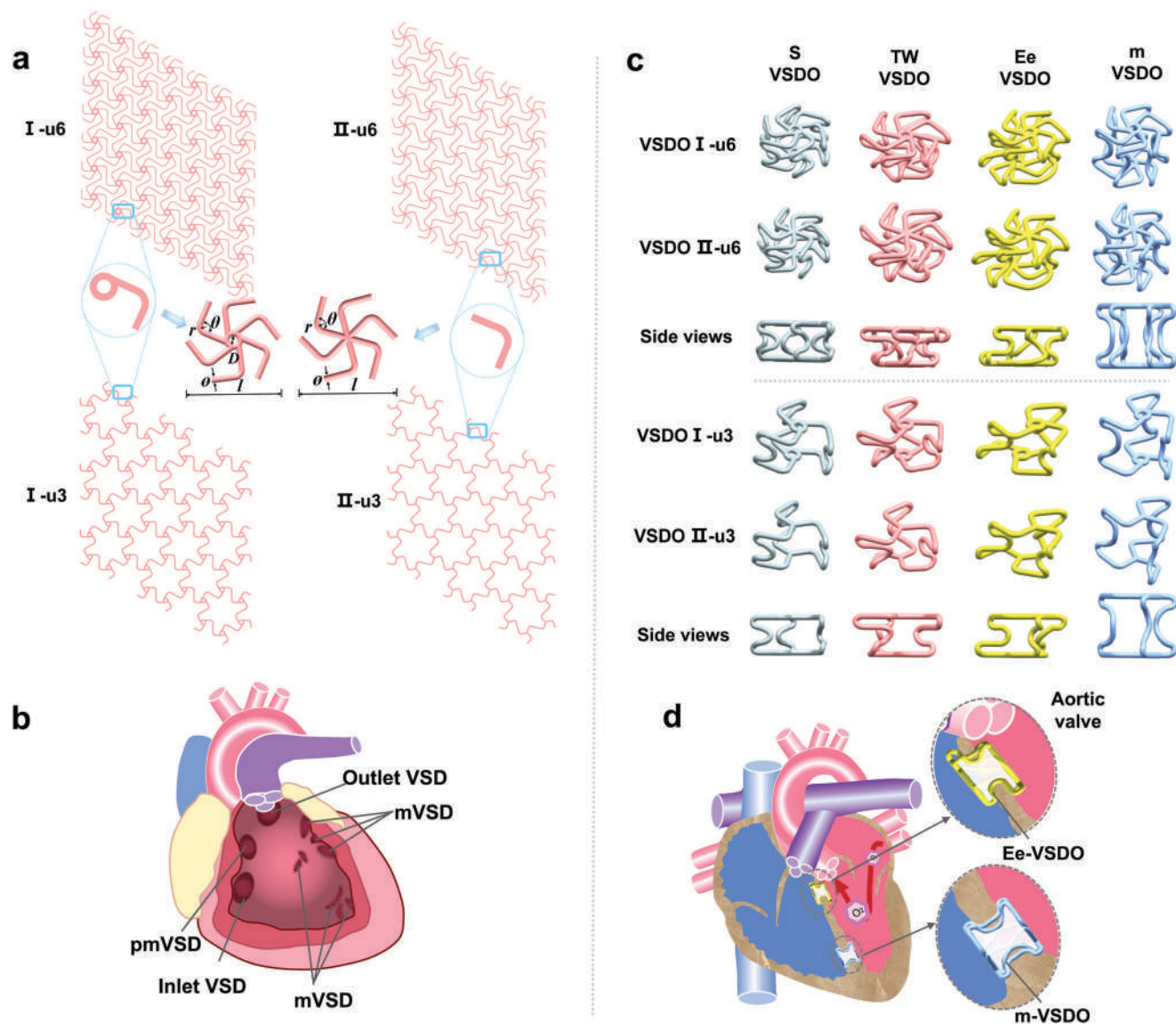
Figure 5. a) Wavy networks and geometric parameters of representative units. b) Classification of ventricular septal defect (VSD) and the anatomical location of each subtype. c) Three-dimensional (3D) models of different ventricular septal defect occluders (VSDOs.) d) Schematic illustration of VSDs occluded with Ee-VSDO and m-VSDO.

of the overall occluder structure can be achieved. The configurations of symmetric S-VSDO, thin waist TW-VSDO, eccentric Ee-VSDO, and lengthened waist m-VSDO prepared with 5BS-C, 10BS-C, and 15BS-C were clearly visible, and each ligament of the occluder can be easily distinguished.

2.4. Mechanical Performance of 4D Printed Bionic VSDOs

The mechanical properties of VSDOs with different radiopaque filler content and different configurations were evaluated (**Figure 8**a–d). A custom-made fixture with a center hole was used to simulate VSD, and the VSDO was placed in the center of the fixture for tensile testing to assess the waist-bearing capacity of the occluder. Overall, with the increase of BS content, the waist

bearing capacity of the occluders showed a gradually decreasing trend. 5BS-C occluders had the strongest waist bearing capacity, followed by 10BS-C occluders, and the waist bearing capacity of 15BS-C occluders was relatively weak. This was consistent with the tensile test results of the standard samples of the three BS-C biocomposites in Figure 3c–e. At 37 °C, the tensile strength of 5BS-C was the highest, followed by 10BS-C, and the tensile strength of 15BS-C was slightly lower. In addition, the zigzag shape in the curve was caused by the successive destruction of the waist ligaments of the occluder due to the increasing load. Because of the lengthened waist of m-VSDOI occluders, their stability was reduced and their load-displacement curves showed more fluctuation. The maximum load that 5BC-C-S-VSDOI, 10BC-C-S-VSDOI, and 15BC-C-S-VSDOI waist can bear was approximately 30, 23, and 16 N respectively. The load bearing
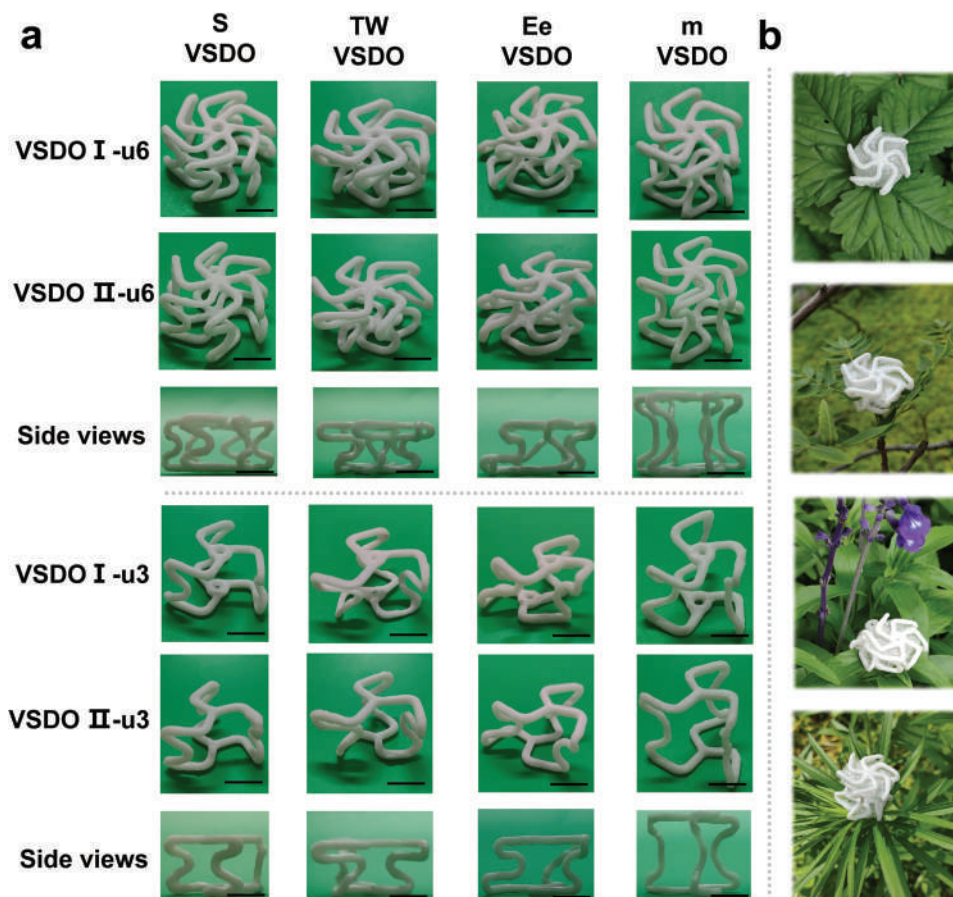
**ADVANCED
SCIENCE NEWS**
www.advancedsciencenews.com

**ADVANCED
HEALTHCARE
MATERIALS**
www.advhealthmat.de

Figure 6. a) Four-dimensional (4D) printed bionic ventricular septal defect occluders (VSDOs) with different configurations. Scale bar: 5 mm. b) Lightweight demonstration of occluders with blocking membranes.

capacity of TW-VSDOI was similar to that of S-VSDOI. The maximum load that the waist of 5BC-C-TW-VSDOI, 10BC-C-TW-VSDOI, and 15BC-C-TW-VSDOI can bear was about 31, 25, and 17 N. The maximum load that the waist of 5BC-C-Ee-VSDOI, 10BC-C-Ee-VSDOI, and 15BC-C-Ee-VSDOI can bear was about 26, 22, and 14 N. The waist bearing capacity of m-VSDOI was weak, which was also caused by the reduced structural stability due to the lengthened waist of m-VSDOI. The maximum load that the waist of 5BC-C-mVSDOI, 10BC-C-mVSDOI, and 15BC-C-mVSDOI can bear was about 21, 17, and 9 N, respectively.

Then, the influences of the ligament structures and the number of ligaments on the waist bearing capacity of the occluders were explored (Figure 8e–h). It can be seen that the mechanical properties of the occluders were less affected by the structure of ligaments (type I and II), but more significantly affected by the number of ligaments. Taking 5BC-C-TW-VSDO as an example, the waist bearing capacity of 5BC-C-TW-VSDOI and 5BC-C-TW-VSDOII was about 32 and 31 N, respectively, while the waist bearing capacity of 5BC-C-TW-VSDOI-u3 was only about 10 N. The other three types of occluders also showed similar results. On the whole, the waist bearing capacity of the type I-three ligament occluder (VSDO I-u3) was between 8 and 10 N, while that of the type I-six ligament occluder (VSDO I) was 2–3 times higher. After

30 days of degradation, the waist bearing capacities of S-VSDOI, TW-VSDOI, and Ee-VSDOI prepared by 5BS-C were about 17, 18, and 18 N, respectively (Figure 8i–k). While the waist-bearing capacity of m-VSDO was lower, approximately 10 N (Figure 8l). In addition, the compression performance of different occluders was investigated, and the maximum compression load was set as 100 N (Figure 8m–p). With the increase of the radiopaque filler content, the capacity of the occluder to bear the compressive load gradually decreased. The m-VSDO exhibited a lower compression load carrying capacity than the S-VSDO, TW-VSDO, and Ee-VSDO, which was also due to its longer waist and reduced structural stability.

2.5. Biocompatibility of 4D Printed Bionic VSDOs

Based on the above results, 5BS-C VSDOs showed overall radiopacity and excellent mechanical strength, and therefore 5BS-C VSDOs were implanted into mice to examine the in vivo histocompatibility (**Figure 9**a). After the operation, host mice underwent a foreign body reaction for self-protection.[34,35] The inflammatory response was most intense within 7 days after the operation, a process commonly referred to as the acute response stage. In Figure 9b (7 days), many inflammatory cell infiltration
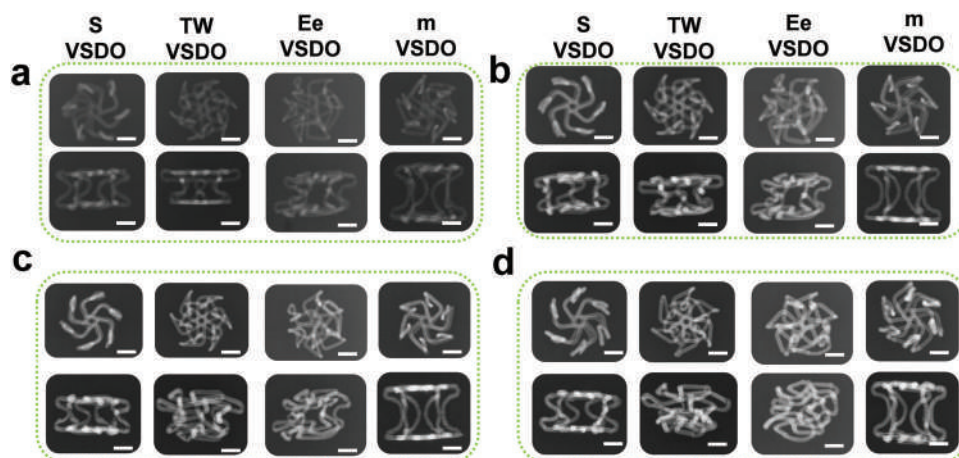
ADVANCED
SCIENCE NEWS
www.advancedsciencenews.com

ADVANCED
HEALTHCARE
MATERIALS
www.advhealthmat.de

Figure 7. Ex vivo overall radiopacity of four-dimensional (4D) printed bionic ventricular septal defect occluders (VSDOs) with different radiopaque filler contents. a) Polyethylene glycol (PEG)/polylactic acid (PLA) matrix (0BS-C). b) 5BS-C, c) 10BS-C, and d) 15BS-C. Scale bar: 5 mm.
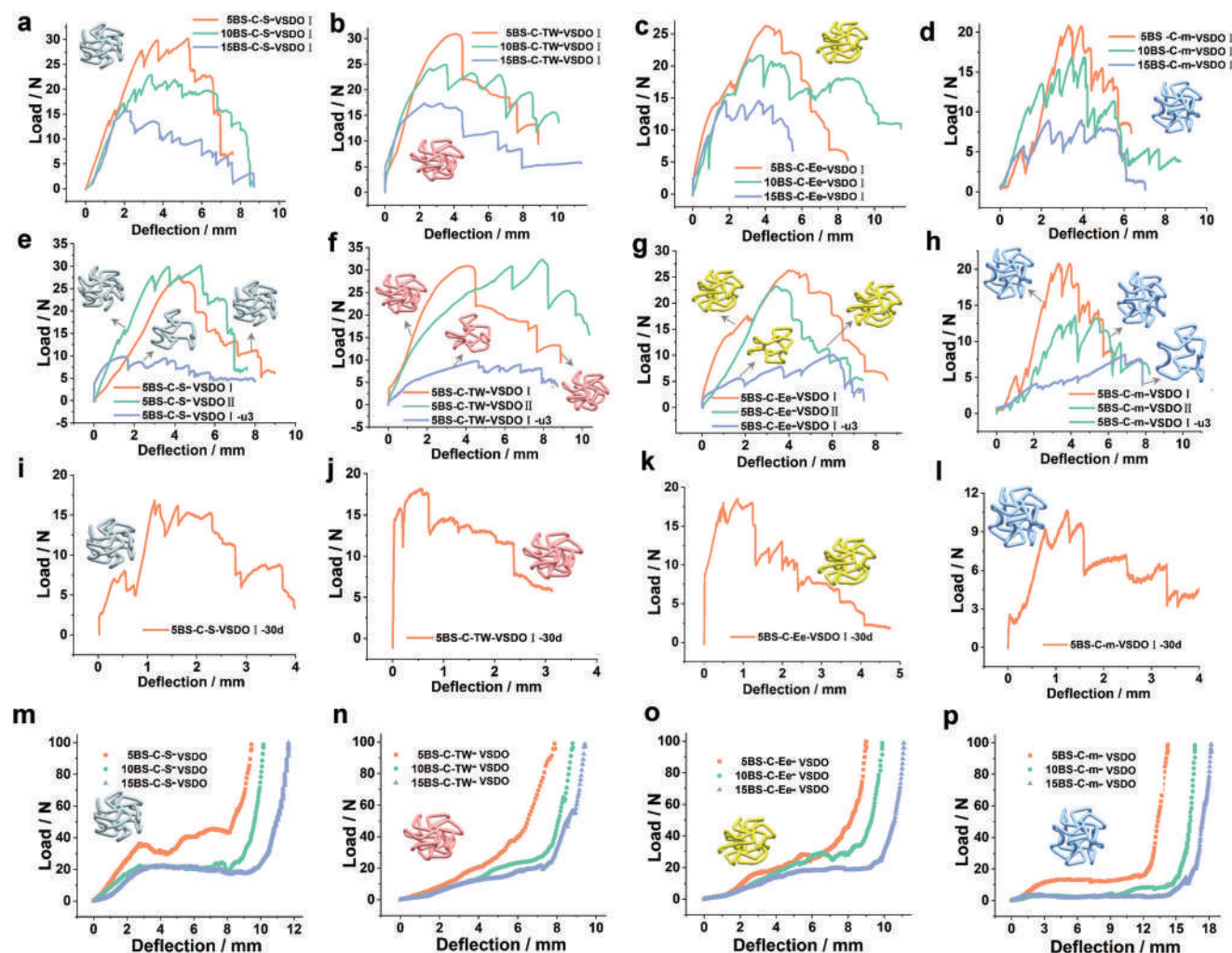

Figure 8. a–d) Tensile tests of VSDOIs with different BS contents. a) S-VSDO, b) TW-VSDO, c) Ee-VSDO, d) m-VSDO. e–h) Tensile tests of 5BS-C-VSDOs with different ligament structures and numbers. e) S-VSDO, f) TW-VSDO, g) Ee-VSDO, h) m-VSDO. i–l) Tensile tests of 5BS-C-VSDOIs after degradation for 30 days. i) S-VSDO, j) TW-VSDO, k) Ee-VSDO, l) m-VSDO. m–p) Compression tests of VSDOIs with different BS contents. m) S-VSDOI, n) TW-VSDOI, o) Ee-VSDOI, and p) m-VSDOI.
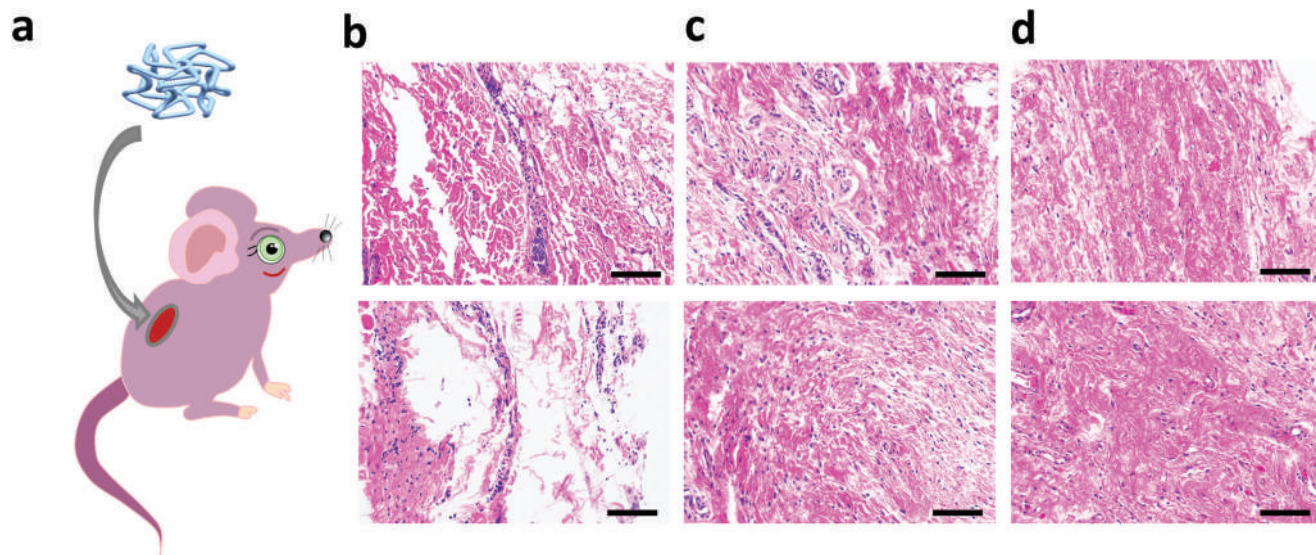
Figure 9. a) Schematic diagram of implanting ventricular septal defect occluders (VSDOs) into mice. Hematoxylin and eosin (HE) staining of tissue around 5BS-C VSDOs after different implantation times b) 7 days, c) 30 days, and d) 60 days. Scale bar: 100 µm.
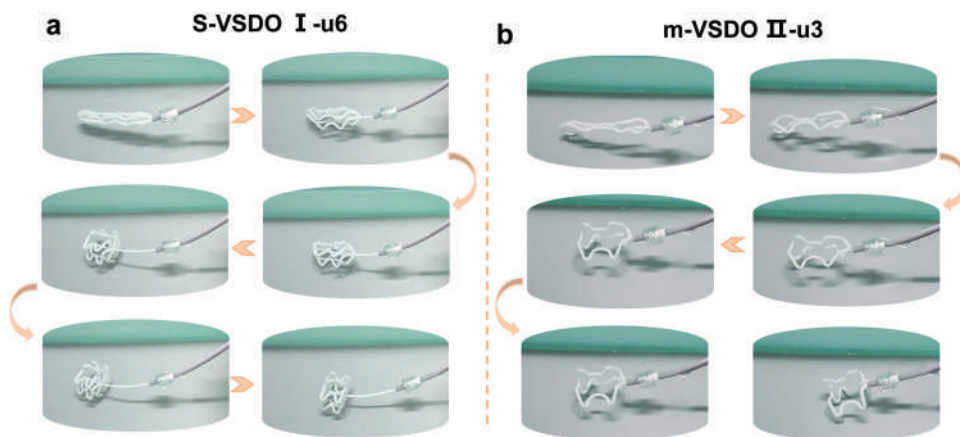

Figure 10. Dynamic shape transformation behaviors of a) S-VSDOI-u6 and b) m-VSDOII-u3.

can be observed, and fibrosis tissues were in a loose state. As time increased, the inflammatory response gradually subsided and the host entered the stage of chronic response. At 30 days, inflammatory cells were significantly reduced. At 60 days, the inflammation continued to subside and dense fibrosis tissues appeared, demonstrating biocompatibility (Figure 9c,d).[36–38]

2.6. Dynamic Shape Transformation Performance and In Vivo Overall Radiopacity

The dynamically reconfigurable shape transformation and self-adaptive deployment of VSDOs were examined (**Figure 10**). The S-VSDOI-u6 and m-VSDOII-u3 occluders with different ligament structures and ligament numbers can be endowed with a temporary configuration of a small cross-sectional area under external stimulation, which was conducive to minimally invasive implantation. The VSDOs in the temporary configuration

automatically and orderly recovered to the original double-disc configuration upon reheating, demonstrating excellently programmable and reconfigurable shape memory performance.

Then, VSDOs were implanted in rabbits to examine the overall radiopacity in vivo. Under the interference of biological tissues, 0BS-C VSDO was difficult to be distinguished, while the 5BS-C VSDO, 10BS-C VSDO, and 15BS-C VSDO can all be accurately positioned after loading radiopaque fillers. Under X-ray, not only the different configurations of VSDOs can be fully displayed, even the ligaments of VSDOs can be clearly identified (**Figure 11**).

3. Conclusion

In summary, we proposed a facile yet versatile strategy to prepare 4D printed bionic VSDOs with customized configuration, biodegradability, biocompatibility, overall radiopacity, and
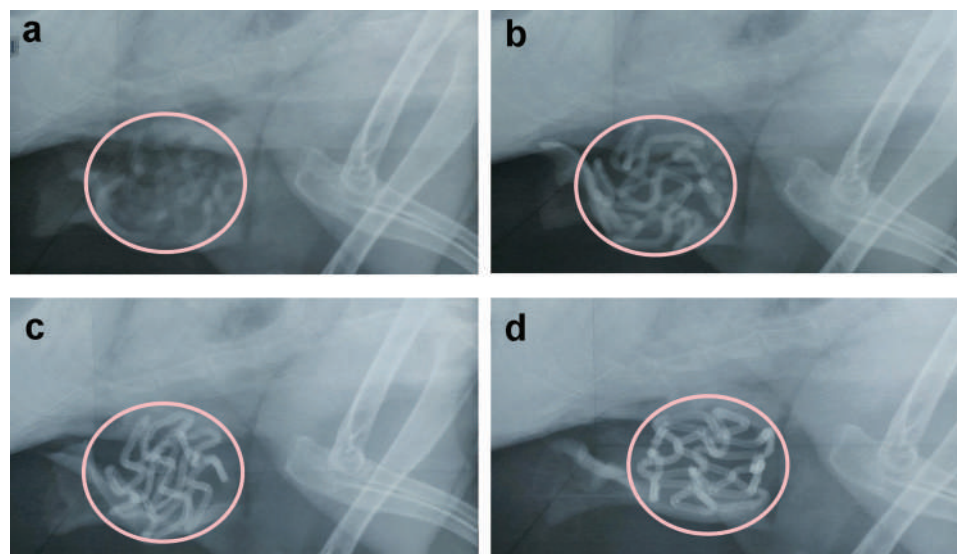
Figure 11. In vivo overall radiopacity examination by implanting ventricular septal defect occluders (VSDOs) into rabbits. a) 0BS-C, b) 5BS-C, c) 10BS-C, and d) 15BS-C.

dynamically reconfigurable deployment. These novel 4D printed bionic occluders provide a feasible solution for the wear, displacement, perforation, and embolism caused by the alloy occluders, and can completely avoid late complications. The overall radiopacity of occluders can avoid inaccurate positioning caused by only a few radiopaque markers of the alloy occluders, and was conducive to precise intraoperative positioning and postoperative follow-up monitoring. More importantly, the 4D printed shape memory radiopaque biocomposite filaments and VSDOs were suitable for scale-up production, providing the possibility of clinical application of occluders.

Moving forward, it is necessary to occlude VSD in vivo and evaluate the long-term efficacy of the 4D printed occluders. In addition, with the developed biodegradable, biocompatible, and overall radiopaque 4D printed filaments, the application scope of this manufacturing process can be expanded to prepare other intelligent medical devices, including various tissue engineering scaffolds and drug delivery devices. The device preparation strategy of this work is integrated with the zeitgeist of personalized medicine, ensuring on-demand, on-site production of customized medical devices.

4. Experimental Section

Overall Radiopaque 4D Printed Filament Fabrication: The mass fraction ratio of PLA granules (Nature Works LLC. Ingeo) and PEG1500 (Sinopharm Chemical Reagent Co., Ltd.) was 8:2, and $BaSO_4$ (2 μm, Aladdin) accounted for 5, 10, and 15 wt% of the total mass of all components, respectively. Firstly, PLA, PEG, and $BaSO_4$ with a specific composition ratio were physically mixed in a vibrating mixer and then ground with a grinder. Subsequently, the mixture was processed by hot melt extrusion, and filaments were prepared by a co-rotating twin-screw extrusion machine (CTE20 PLUS). The ratio of extruder screw length to barrel diameter (L/D ratio) was 50:1. The extruder was equipped with nine individually regulated heating zones, where temperatures were set between 175 °C and 190 °C. The mixture passed through nine heating zones in a sequence, fully mixed, and melted. Finally, the rotating screw fed the mixture to the round die head with a diameter of 1.75 mm. The winder speed and the puller speed were specially adjusted to match each other to ensure a constant filament diameter of 1.75 ± 0.05 mm.

Design and Fabrication of 4D Printed Constructs: The digital models of the constructs were built on UG NX 10.0 software, and the. STL files of digital models were exported to Allcct slice software (Allcct, Wuhan, China). Each model was sliced, and the building paths were automatically generated. The .gcode file containing the build path was connected to the FDM printer, and the construct was printed layer by layer. The print head temperature and print speed were 195 °C and 10 mm s^{-1} respectively, and the hotbed temperature was set to 40 °C.

Mechanical Testing: Uniaxial tensile tests were performed according to ASTM D638. A universal electronic tensile tester (Zwick, GmbH) with a 1 kN load cell was employed for testing at a constant loading rate of 2 mm min^{-1}. The flexural performance of the BS-C was characterized on the tester equipped with a three-point bending clamp, and the tests were performed following the ASTM D790 with a loading rate of 2 mm min^{-1}. The compression tests of VSD occluders were carried out by placing the occluders between the upper and lower compression fixtures, and the tests were conducted at the same loading rate. All of the tests were performed at 37 °C (body temperature). Prior to testing, the sample was placed in a heating cabinet associated with the tester and heated from room temperature to 37 °C at a rate of 3 °C min^{-1} and then kept for another 15 min to ensure that the sample reached thermal equilibrium. Three replicates were set for each sample and the average was exported.

Ex Vivo Degradation Evaluation: Phosphate buffer solution (PBS) was chosen as the degradation medium due to its similarity with human body fluids. The samples to be evaluated were completely immersed in the degradation medium and cultured in an incubator at 37 °C. At predetermined times, the samples were taken out, rinsed, and dried thoroughly, and then weighed and tested. The degradation media were replaced every 7 days to maintain the pH value (7.2–7.4). The weight loss was calculated according to:

$$\text{Weight loss } (\%) = -\frac{w_t - w_0}{w_0} \times 100\% \qquad (1)$$

where w_0 was the dry weight before degradation, and w_0 was the dry weight at time t.

DSC Analysis: DSC was carried out via a TA Q200 instrument, with nitrogen as the protective atmosphere. For each measurement,

**ADVANCED
SCIENCE NEWS**

www.advancedsciencenews.com

**ADVANCED
HEALTHCARE
MATERIALS**

www.advhealthmat.de

approximately 7 mg of BS-C sample was loaded onto the aluminum pan and heated from room temperature to 200 °C at a rate of 5 °C min^{-1}, then cooled to room temperature at the same rate. The first heating/cooling cycle was used to erase thermal history. Finally, the sample was heated again in the same way and the obtained data was derived.

FT-IR Measurement: The FT-IR measurement was performed with Bruker Tensor 27 instrument. The samples were analyzed in absorbance mode in the range of 4000–400 cm^{-1}, and each spectrum was collected by 32 scans with a resolution of 4 cm^{-1}. The functional groups corresponding to each absorption band were analyzed.

In Vivo Biocompatibility: The animal experiments were approved by the ethics committee of the First Affiliated Hospital of Harbin Medical University (2021024). In vivo biocompatibility was assessed by subcutaneous implantation of sterile VSDOs into Sprague Dawley (SD) male mice, and histological analysis was performed on tissue sections. To avoid effects on the normal life of the mice, reduced-volume VSDOs of approximately 10 mm in diameter and 3 mm in height were implanted. Fifteen adult male SD mice (150–200 g) were euthanized at 7, 30, and 60 days, postoperatively ($n = 3$), and BS-C, as well as surrounding adhesive tissues, were collected. The VSDOs and tissues were soaked in 10% formalin for 24 h for fixation and then embedded in the embedding machine. The tissue slices with a thickness of 4 µm were obtained using a slicer, and then the drying and dewaxing procedures were performed. The tissue was stained with hematoxylin and eosin successively, and the tissue sections were analyzed under an inverted optical microscope (Olympus, Japan). In addition, the main organs (lung, liver, spleen, kidney, and heart) of mice were sectioned and histologically evaluated by the same method.

Dynamic Shape Transformation Performance: To program the printed construct, the construct was first immersed in a hot water bath (Tg + 20 °C) for 180 s, and then the construct was programmed to the target temporary configuration through an external load. The temporary configuration was stabilized by cooling to room temperature while maintaining the external load. The shape transformation process was carried out on a digital display heating platform at a temperature of 43 °C. The construct in the temporary configuration was reheated and automatically recovered to its original configuration.

Overall Radiopacity Assessment: The overall radiopacity of VSDOs ex vivo and in vivo was examined using an X-ray Imaging System (Philips Medical System). Ex vivo radiopacity was imaged by placing VSDOs with different radiopaque filler contents directly on the imaging platform. In vivo radiopacity was examined by implanting VSDOs into four 6-month-old male New Zealand White rabbits. The New Zealand White rabbits weighed approximately 3.0 kg and were housed in a standard specific pathogen-free (SPF) laboratory. After anesthesia, an oblique incision was made in the lower left anterior thorax of the rabbit under aseptic conditions. The intercostal muscles and connective tissues were separated; the pericardial cavity was opened and VSDOs were implanted. Then, the rabbits implanted with VSDOs were examined under X-ray to assess the overall radiopacity of the VSDOs under in vivo tissue interference.

Supporting Information

Supporting Information is available from the Wiley Online Library or from the author.

Acknowledgements

Conflict of Interest

The authors declare no conflict of interest.

Data Availability Statement

The data that support the findings of this study are available from the corresponding author upon reasonable request.

Keywords

[1] S. Glen, J. Burns, P. Bloomfield, *Heart* **2004**, *90*, 1321.
[2] C. Lin, L. Liu, Y. Liu, J. Leng, *Acta Biomater.* **2021**, *128*, 100.
[3] J. E. Lock, P. C. Block, R. G. Mckay, D. S. Baim, J. F. Keane, *Circulation* **1988**, *78*, 361.
[4] J. Yang, L. Yang, Y. Wan, J. Zuo, J. Zhang, W. Chen, J. Li, S. Yu, J. Liu, T. Chen, W. Duan, L. Xiong, D. Yi, *Eur. Heart J.* **2010**, *31*, 2238.
[5] Q. Wang, X. Zhu, Z. Duanzhen, P. Zhang, H. Chen, X. Han, X. Sheng, L. Meng, *J. Card. Surg.* **2017**, *32*, 370.
[6] M. Shrestha, W. Promphan, T. Layangool, S. Roymanee, K. Wongwaitaweewong, P. Prachasilchai, T. Kirawittaya, C. Sangtawesin, P. Pattarakunwiwat, *Catheter. Cardiovasc. Interventions* **2019**, *93*, E30.
[7] Y. Qin, J. Chen, X. Zhao, D. Liao, R. Mu, S. Wang, H. Wu, H. Guo, *Am. J. Cardiol.* **2008**, *101*, 1781.
[8] E. Odemis, M. Saygi, A. Guzeltas, I. C. Tanidir, Y. Ergul, I. Ozyilmaz, I. Bakir, *Pediatr. Cardiol.* **2014**, *35*, 817.
[9] R. Mijangos-Vazquez, A. El-Sisi, J. J. Sandoval, J. A. Garcia-Montes, R. Hernandez-Reyes, R. Sobhy, A. Abdelmassih, M. M. Soliman, S. Ali, T. Molina-Sanchez, C. Zabal, *J. Interventional Cardiol.* **2020**, *2020*, 8948249.
[10] K. D. Mandal, D. Su, Y. Pang, *Front. Pediatr.* **2018**, *6*, 128.
[11] Y. Huang, J. F. Kong, S. S. Venkatraman, *Acta Biomater.* **2014**, *10*, 1088.
[12] C. Lin, J. Lv, Y. Li, F. Zhang, J. Li, Y. Liu, L. Liu, J. Leng, *Adv. Funct. Mater.* **2019**, *29*, 1906569.
[13] C. Lin, L. Liu, Y. Liu, J. Leng, *ACS Appl. Mater. Interfaces* **2021**, *13*, 12668.
[14] O. Elkiran, C. Karakurt, G. Kocak, C. Taskapan, *Cardiol. Res. Pract.* **2019**, *2019*, 7891746.
[15] F. J. Hernández Pérez, J. A. Fernández Díaz, C. García Montero, A. García Touchard, J. F. Oteo Domínguez, J. R. Domínguez Puente, J. Goicolea Ruigómez, *EuroIntervention* **2013**, *9*, 532.
[16] S. Gielen, F. T. Riede, G. Schuler, I. Dahnert, *Catheter. Cardiovasc. Interventions* **2012**, *79*, 1161.
[17] D. N. Lysitsas, B. Wrigley, P. Banerjee, P. E. Glennon, J. M. Parmar, M. F. Shiu, M. Been, *Int. J. Cardiol.* **2009**, *131*, e106.
[18] T. K. Jones, L. A. Latson, E. Zahn, C. E. Fleishman, J. Jacobson, R. Vincent, K. Kanter, *J. Am. Coll. Cardiol.* **2007**, *49*, 2215.
[19] L. M. Ruiz, J. M. de la Torre-Hernandez, J. Zueco, N. J. Francisco, *Rev. Esp. Cardiol.* **2007**, *60*, 451.
[20] B. Wertman, B. Azarbal, M. Riedl, J. Tobis, *J. Am. Coll. Cardiol.* **2006**, *47*, 1226.
[21] T. Cotts, P. J. Strouse, J. N. Graziano, *Catheter. Cardiovasc. Interventions* **2006**, *68*, 754.
[22] Z. Amin, Z. M. Hijazi, J. L. Bass, J. P. Cheatham, W. E. Hellenbrand, C. S. Kleinman, *Catheter. Cardiovasc. Interventions* **2004**, *63*, 496.

[23] M. Chessa, M. Carminati, G. Butera, R. M. Bini, M. Drago, L. Rosti, A. Giamberti, G. Pome, E. Bossone, A. Frigiola, *J. Am. Coll. Cardiol.* **2002**, *39*, 1061.

[24] X. Huang, Y. Zhu, J. Cao, J. Hu, Y. Bai, H. Jiang, Z. Li, Y. Chen, W. Wang, Y. Qin, *Catheter. Cardiovasc. Interventions* **2013**, *81*, 324.

[25] H. Cui, C. Liu, T. Esworthy, Y. Huang, Z. Yu, X. Zhou, H. San, S. Lee, S. Y. Hann, M. Boehm, M. Mohiuddin, J. P. Fisher, L. G. Zhang, *Sci. Adv.* **2020**, *6*, b5067.

[26] D. You, G. Chen, C. Liu, X. Ye, S. Wang, M. Dong, M. Sun, J. He, X. Yu, G. Ye, Q. Li, J. Wu, J. Wu, Q. Zhao, T. Xie, M. Yu, H. Wang, *Adv. Funct. Mater.* **2021**, 2103920.

[27] C. Lin, L. Liu, Y. Liu, J. Leng, *Compos. Struct.* **2022**, *279*, 114729.

[28] Y. Deng, F. Zhang, M. Jiang, Y. Liu, H. Yuan, J. Leng, *ACS Appl. Mater. Interfaces* **2022**, *14*, 42568.

[29] F. Zhang, N. Wen, L. Wang, Y. Bai, J. Leng, *Int. J. Smart Nano Mater.* **2021**, *12*, 375.

[30] C. Lin, L. Liu, Y. Liu, J. Leng, *Int. J. Smart Nano Mater.* **2020**, *11*, 24.

[31] Y. Xia, Y. He, F. Zhang, Y. Liu, J. Leng, *Adv. Mater.* **2021**, *33*, 2000713.

[32] L. Jiang, J. Zhang, M. P. Wolcott, *Polymer* **2007**, *48*, 7632.

[33] C. Spies, Q. L. Cao, Z. M. Hijazi, *Eur. Heart J. Suppl.* **2010**, *12*, E24.

[34] E. Fournier, C. Passirani, C. N. Montero-Menei, J. P. Benoit, *Biomaterials* **2003**, *24*, 3311.

[35] Y. Ramot, M. Haim-Zada, A. J. Domb, A. Nyska, *Adv. Drug Delivery Rev.* **2016**, *107*, 153.

[36] H. L. Yang, Z. Zhang, C. Gao, Y. Bai, B. Liu, W. Wang, Y. Ma, Saijilafu, Y. Li, A. Chan, L. Yang, *Mater. Sci. Eng., C* **2020**, *116*, 110904.

[37] J. W. Hoekstra, J. J. van den Beucken, S. C. Leeuwenburgh, E. M. Bronkhorst, G. J. Meijer, J. A. Jansen, *J. Biomed. Mater. Res., Part A* **2014**, *102*, 141.

[38] E. A. Bortoluzzi, C. Silveira Teixeira, N. J. Broon, A. Consolaro, T. N. Pinheiro, L. Fonseca Roberti Garcia, D. H. Pashley, C. M. Bramante, *Microsc. Res. Tech.* **2021**, *84*, 705.